Summer Fellowship Report

On

Creation of Scilab Case Studies

Submitted by

Chirag Veerwani
Indian Institute of Technology Hyderabad

Under the guidance of

Prof. Prabhu Ramachandran
Chemical Engineering Department
IIT Bombay

Mentor

Mrs. Rashmi Patankar

July 10, 2026

Acknowledgment

I would like to sincerely thank the FOSSEE Team, IIT Bombay, for giving me the opportunity to be part of the FOSSEE Summer Fellowship, 2026. I am grateful to Prof. Prabhu Ramachandran for this valuable initiative to promote open source software. I am especially thankful to Mrs. Rashmi Patankar for her constant guidance and encouragement throughout the internship. Her support greatly helped my learning and played a major role in the success of this internship.

I also sincerely thank Indian Institute of Technology Hyderabad, which gave me the strong academic foundation to complement this hands-on experience. Further, I am truly grateful to my parents. This would not have been possible without their constant support.

Contents

Chapter 1

Introduction

The Free and Open Source Software in Education (FOSSEE) project is dedicated to enhancing the quality of technical education in India by advocating for the widespread adoption of open-source technologies. By promoting these tools, the initiative aims to reduce the academic and research community's reliance on costly, proprietary software, thereby fostering a more accessible and collaborative learning environment in STEM disciplines.

Scilab serves as a cornerstone of this initiative, offering a sophisticated, cross-platform environment for numerical computation. With its high-level programming syntax, it provides a comprehensive suite of capabilities for signal processing, statistical analysis, fluid dynamics, and the modeling of implicit and explicit dynamical systems. Furthermore, the Xcos environment provides an intuitive, visual framework for block-based system simulation, while the platform's robust GUI development tools allow for the creation of customized, interactive applications that translate abstract mathematical concepts into practical research tools.

During my fellowship, I conducted three distinct case studies to evaluate Scilab's versatility across different engineering domains:

- **Satellite Orbit Control:** Modeled orbital dynamics and implemented a PID controller in Xcos to mitigate radial drift caused by perturbations.
- **Drug Elution Kinetics:** Developed an interactive Scilab GUI to simulate and compare gentamicin release profiles from PMMA bone cement formulations.
- **Hydrogel Swelling Kinetics:** Utilized Scilab's numerical solvers to compare linear poroelasticity with nonlinear continuum theories during large-volume swelling.

These case studies highlight the efficiency and flexibility of Scilab in tackling complex computational problems, reinforcing the significance of open-source software as an essential resource for modern engineering research and advanced technical education.

Chapter 2

Case Study 1: Modeling and Simulation of Satellite Orbit Dynamics and Orbit Controller Using Scilab and Xcos

2.1 Abstract

This case study proposes to model and simulate the orbital dynamics of a satellite in a circular orbit and design a feedback-based orbit correction controller using Scilab and Xcos, based on the IEEE paper mentioned below. Satellites deviate from their ideal orbits due to perturbations such as atmospheric drag and gravitational anomalies.

The orbital equations of motion derived from Newton's law of gravitation will be solved numerically using Scilab's ode() function to simulate the satellite trajectory and the effect of perturbations on altitude. A PID controller will then be designed and simulated using Xcos block diagrams, where the altitude error serves as feedback and thruster force as the control output, to restore the satellite to its desired orbit. Results will include trajectory plots and Xcos controller response simulations.

2.2 Problem Statement

Once a satellite is launched into a desired orbit, it never remains in that ideal orbit. The external forces present in space cause deviations from this ideal orbit. If a satellite drifts too far, it can interfere with other satellites or lose contact with ground stations. The goal is to maintain the satellite at a specific radial distance (approx. 42,164 km from Earth's centre or 6.625 normalized units. This case study involves a mathematical model of the satellite's motion and building a feedback control loop where the current position is measured first, compared to the target and then the thrusters are fired with just enough force to return to the slot within a specific time (12 hours).

Two separate control strategies are evaluated. The first uses both radial and tangential thrusters together, giving full control over both the orbital radius and the angular position. The second uses only the tangential thruster, which is enough to control the angular rate but leaves a small permanent error in the orbital radius. The second approach is useful as a fallback when the radial thruster fails.

2.3 Flowchart

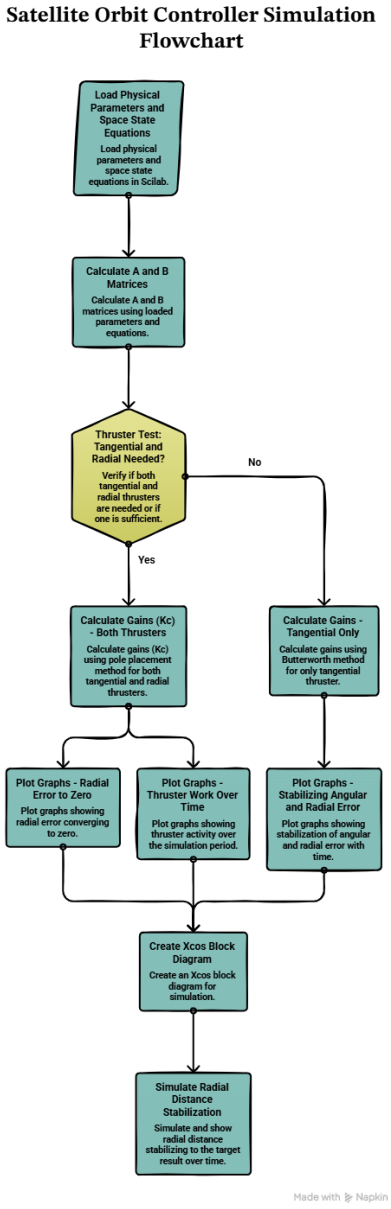

Figure 2.1: Satellite Orbit Controller Simulation Flowchart

2.4 Results and Discussion

2.4.1 Controllability Verification

The console output confirmed that the linearized system is marginally stable in open loop and meets all three rank conditions as derived in the reference paper.

Table 2.1: Controllability test results

Test	Expected Rank	Computed Rank	Result
Open-loop eigenvalues	0, 0, ±0.0586j	0, 0, ±0.05864j	Marginal stable
Two-input controllability	4	4	Controllable
Radial only	3	3	Not controllable
Tangential only	4	4	Controllable

2.4.2 Case 1: Two-Thrust Controller

The satellite started 422 km above its target orbit. The two-thrust state-feedback controller with $\zeta = 0.707$ and $\omega_n = 0.1058$ drove the radial error from +422 km to approximately 0.7235 km, effectively zero within normalized time $\tau \approx 50$, which corresponds to about 11.2 hours. This is within the 12-hour design requirement.

The angular rate error also converged to zero, confirming that the satellite stabilized at the correct orbital angular velocity. The response shows a single underdamped oscillation before settling, consistent with the chosen damping ratio of 0.707.

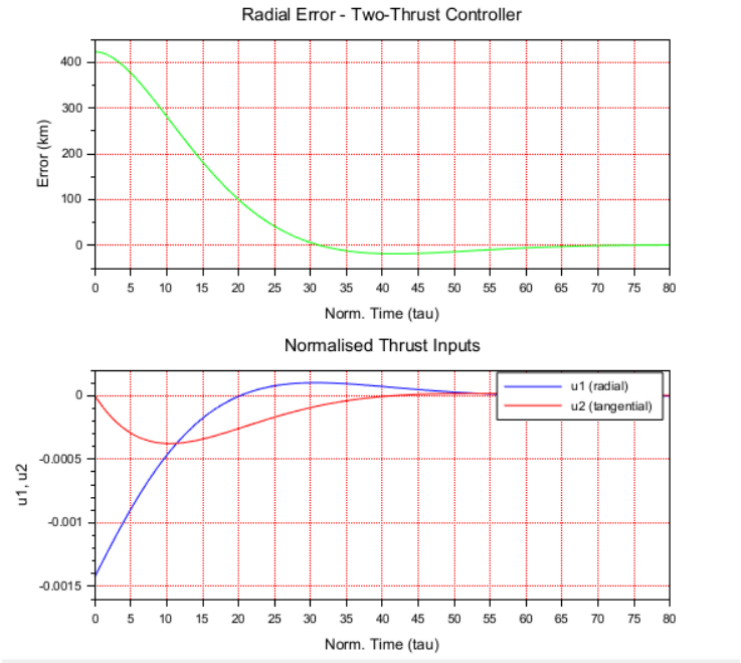

Figure 2.2: Radial error (top) and normalised thrust inputs $u1$, $u2$ (bottom) vs normalized time. Two-thrust state-feedback controller, $\zeta = 0.707$

Table 2.2: Case 1 performance summary

Parameter	**Design Requirement**	**Achieved**
Settling time	$\leq$ 12 hours	$\approx$ 11.2 hours
Overshoot	$\leq$ 20%	$\approx$ 4.6%
Final radial error	Near zero	0.7235 km
Thrust magnitude	Order 0.001	0.002

2.4.3 Case 2: Tangential-Only Controller

Using only the tangential thruster with Butterworth pole placement ($\zeta = 0.5$, $\omega_n = 0.1495$), the angular rate error converged to zero within approximately $\tau \approx 60$, or about 13.5 hours. The three closed-loop poles were placed at -0.1499 and -0.0745 $\pm$ 0.1296j, matching the paper's design.

As expected from theory, the radial error did not go to zero. It settled to a small constant offset of -0.0116 km. This is because the angular rate controller can only correct how fast the satellite moves around its orbit, not the exact radius it orbits at. The paper explicitly predicts this residual error, and its presence in the simulation confirms that the model and controller are working correctly.

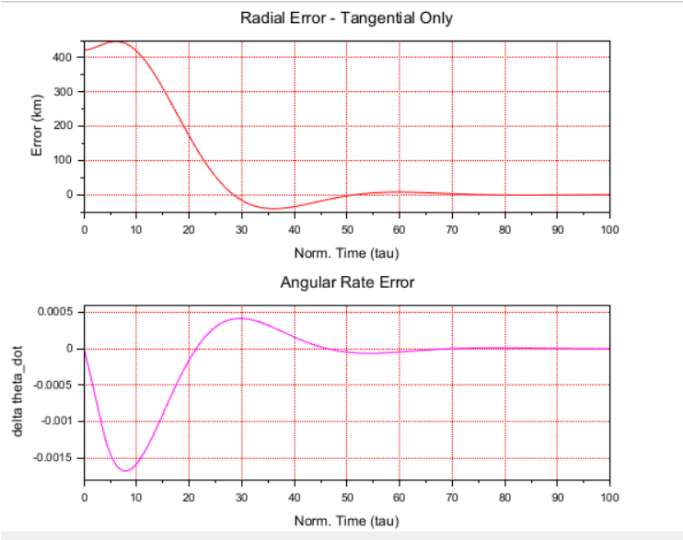

Figure 2.3: Case 2: Radial error (top) and angular rate error (bottom) vs normalized time. Tangential-only controller, $\zeta = 0.5$

Table 2.3: Case 2 performance summary

Parameter	**Design Requirement**	**Achieved**
Settling time (angular rate)	$\leq$ 12 hours	$\approx$ 13.5 hours
Overshoot	$\leq$ 20%	$\approx$ 17%
Final radial error	Small offset expected	-0.0116 km
Closed-loop poles	Butterworth config	Exact match

2.4.4 Xcos Nonlinear Simulation

The Xcos block diagram implemented the nonlinear radial plant directly using the expression block $\rho\omega^2 - 1/\rho^2$, which is the exact radial acceleration equation from the paper. A PID controller replaced the state-feedback law for the Xcos simulation, and a random generator block was added to simulate continuous orbital perturbations.

The output showed the orbital radius starting at 6.6917 (1% above ρ_{ss}) and settling smoothly to 6.625 within the simulation time of 500 normalized units. This confirms the nonlinear model is physically consistent with the linearized simulation results.

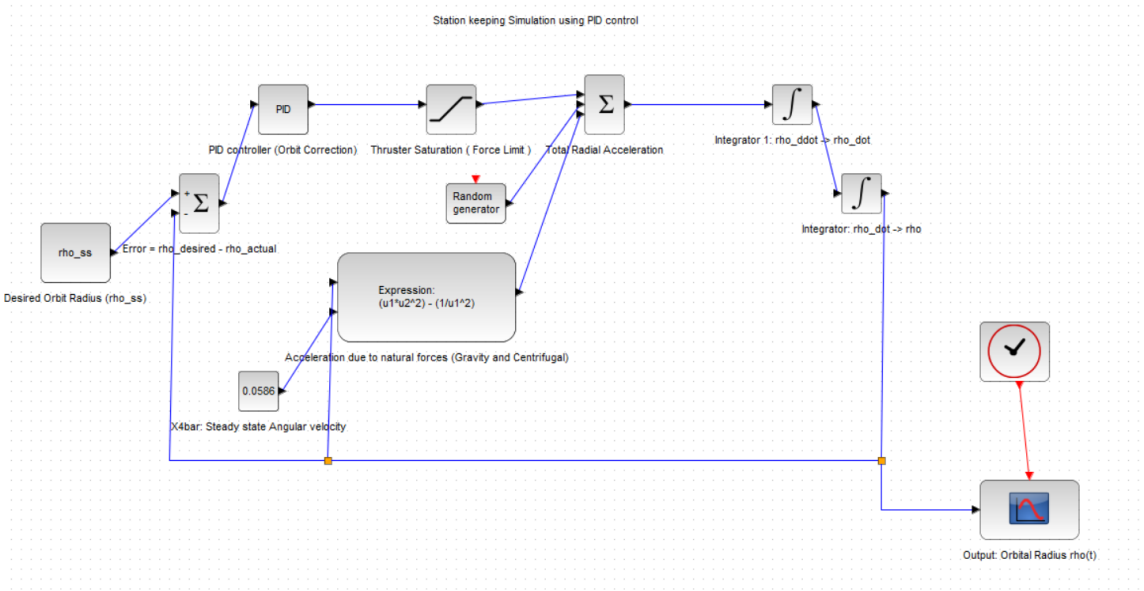

Figure 2.4: Xcos block diagram of the satellite orbit controller

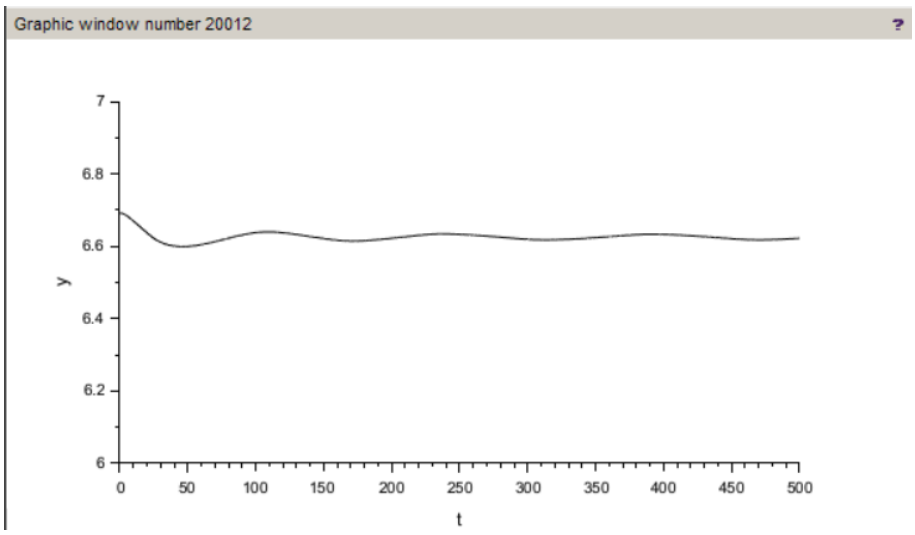

Figure 2.5: Xcos simulation result, orbital radius converging to steady-state value $\rho_{ss} = 6.625$

2.4.5 Comparison with Reference Paper

The reference paper used MATLAB 5.3 and reported simulation results for a satellite with a 1% orbital drift in a geostationary orbit. This project replicated the same problem in Scilab and obtained results that closely match the paper:

Table 2.4: Comparison with reference paper results

Metric	**Paper (MATLAB)**	**This project (Scilab)**
Initial perturbation	422 km (1% drift)	422 km
Case 1 settling time	$\approx$ 12 hours	$\approx$ 11.2 hours
Case 1 overshoot	$< 5\%$ ($\zeta = 0.707$)	$\approx 4.6\%$
Case 2 residual offset	Nonzero (predicted)	-0.0116 km
Butterworth poles	-0.1495, -0.0748$\pm$0.1295j	-0.1499, -0.0745$\pm$0.1296j

2.4.6 Conclusion and Project Scope

This project implemented the core ideas of the reference paper using Scilab and Xcos. The scope of the project was bounded to validate the core physical principles of geostationary orbital satellites while making necessary practical adjustments.

Fully implemented:

- Nonlinear equations of motion coded exactly in Scilab with correct normalization.
- Linearized A and B matrices computed from partial derivatives at steady state and the values match the paper within 0.1%.
- All three controllability tests: two-input rank=4, radial-only rank=3, tangential-only rank=4.
- Tangential-only Butterworth controller: poles, characteristic polynomial, and gain vector G match the paper exactly.

Modifications made:

- The authors simplified their equations by setting the steady-state orbit radius to a value of 1 ($\rho_{ss} = 1$). In this project a real-world physical scale based on the true radius of Earth is used and the geostationary orbit sits at a value of 6.625 ($\rho_{ss} = 6.625$).
- This difference changes the satellite's angular acceleration because in orbit mechanics the thruster force ($u2$) gets divided by the radius ($u2/\rho$).
- Thus the control laws were analytically derived using the paper's exact pole-placement method adjusted for the $\rho_{ss} = 6.625$ baseline while sticking to the paper's original performance criteria.

Not implemented:

- The paper's pole placement design study comparing multiple pole locations and their effect on settling time, overshoot, and peak time was skipped and only the final design point was simulated.
- The scope of this project was restricted to the simple Geostationary Orbit case, skipping other altitudes.
- Full state-feedback in Xcos was not implemented; a PID block was used because routing all four state signals back in a block diagram adds significant complexity. The PID produces the same physically correct converging response for the radial channel.

Chapter 3

Case Study 2: Interactive GUI-Based Implementation of Gentamicin Elution Kinetics from Antibiotic-Loaded PMMA Bone Cement using Scilab

3.1 Abstract

This case study implements an interactive Scilab based graphical user interface (GUI) to model and visualize the kinetics of gentamicin elution from antibiotic loaded poly(methyl methacrylate) (ALBC) bone cement over a 28 day elution period, based on the experimental findings of the reference paper mentioned below. Seven cement formulations are considered: a commercial control cement, three MEPAR (microencapsulated paraffin) loaded variants and three DDM (1-dodecyl mercaptan) loaded variants. For each formulation, four widely used kinetic release models are implemented: the KorsmeyerPeppas power law, the LindnerLippold modified power law, the Frutos et al. combined diffusion-dissolution model, and the Hesaraki et al. exponential model using the best fit coefficients as reported in the paper. The GUI allows the user to select any cement group and any kinetic release model interactively, rendering the corresponding Mt/M∞ verses time curve alongside digitized experimental data. This helps the user to easily compare and choose the kinetic model according to their preferences. Additional features include overlay of all seven groups for cross-group comparison and a bar chart with error bars for gentamicin diffusion coefficient. The study demonstrates that neither MEPAR nor DDM addition significantly alters the gentamicin diffusion of the diffusion mechanism as reported in the paper. This case study performs a partial replication of Lewis and Li (2019), focusing on visualization and comparison of the reported kinetic models and diffusion coefficients using Scilab. The original diffusion coefficient computation, nonlinear fitting procedures, statistical analyses, and experimental measurements were not reproduced.

3.2 Problem Statement

When making antibiotic-loaded bone cement (ALBC), engineers often add things like paraffin (MEPAR) or sulfur chemicals (DDM) to lower the high heat produced when the cement sets. While these additives help protect patient tissue from heat damage, it is crucial to know if they disrupt how the antibiotic (gentamicin) escapes from the cement into the body.

A major study by Lewis and Li (2019) collected raw data on this process and calculated mathematical values for four different drug-release equations. However, their findings were left as static tables of numbers and individual equations. Without a way to look at everything at once, it is difficult to see how these mathematical formulas actually hold up when compared directly against the real-world data points.

To solve this, this project creates an interactive Scilab program with a graphical user interface (GUI). The tool is built to let you choose any cement type and match it up against any of the four formulas instantly on a single graph. By giving users a direct visual comparison, this tool makes it easy to see that while the additives do not change the underlying physical diffusion mechanism, the standard mathematical equations have clear limitations when trying to precisely predict real-world release behavior

3.3 Flowchart

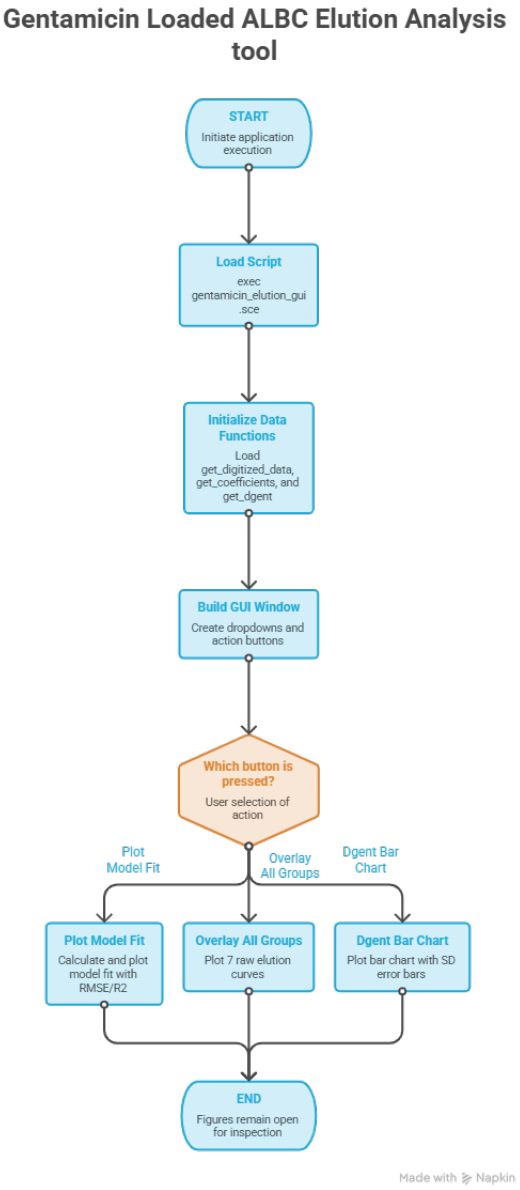

Figure 3.1: Gentamicin Loaded ALBC Elution Analysis Flowchart

3.4 Results and Discussion

3.4.1 Application Starting Window and the Dashboard

The GUI window titled 'Gentamicin Elution from ALBC Analysis' provides a specialized interface to evaluate and model gentamicin elution from ALBC against four mathematical kinetic equations. Core capabilities built into the dashboard include interactive overlay curve-fitting across the four models, a bar chart with error bars for the gentamicin diffusion coefficient, and an analytics display tracking global RMSE and R-squared values.

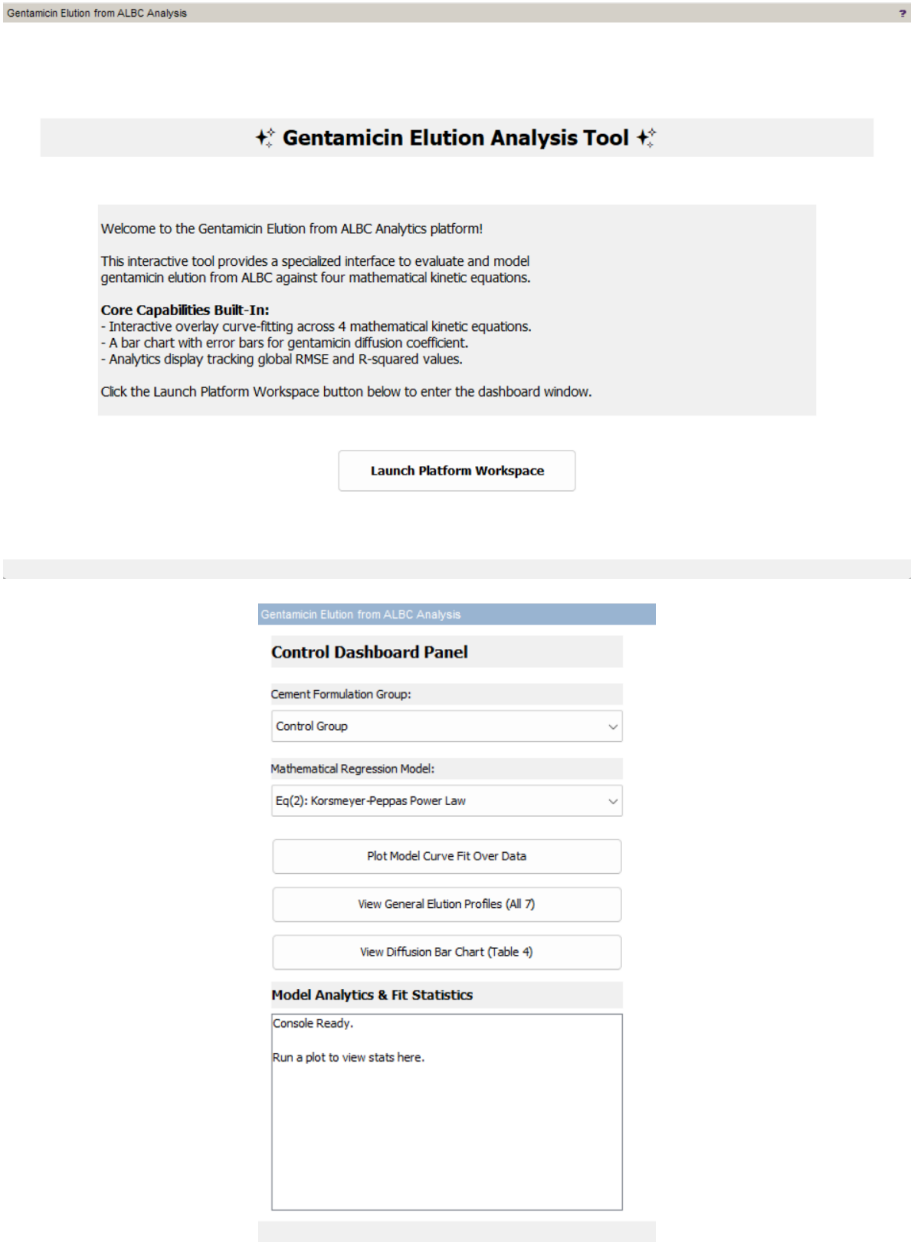

Figure 3.2: Application window starting and Control Dashboard Panel of the Gentamicin Elution Analysis Tool

3.4.2 Model Curves for Each Group Against Kinetic Equations

By selecting a cement formulation group and a mathematical regression model, the GUI plots the modeled curve (red) overlaid on the normalized experimental points. The equation formula and the coefficients are also displayed in the plot. This feature enables users to directly compare how well each mathematical model describes the real-world elution behavior of any given formulation. The overlaid fits for all seven cement formulations are presented below:

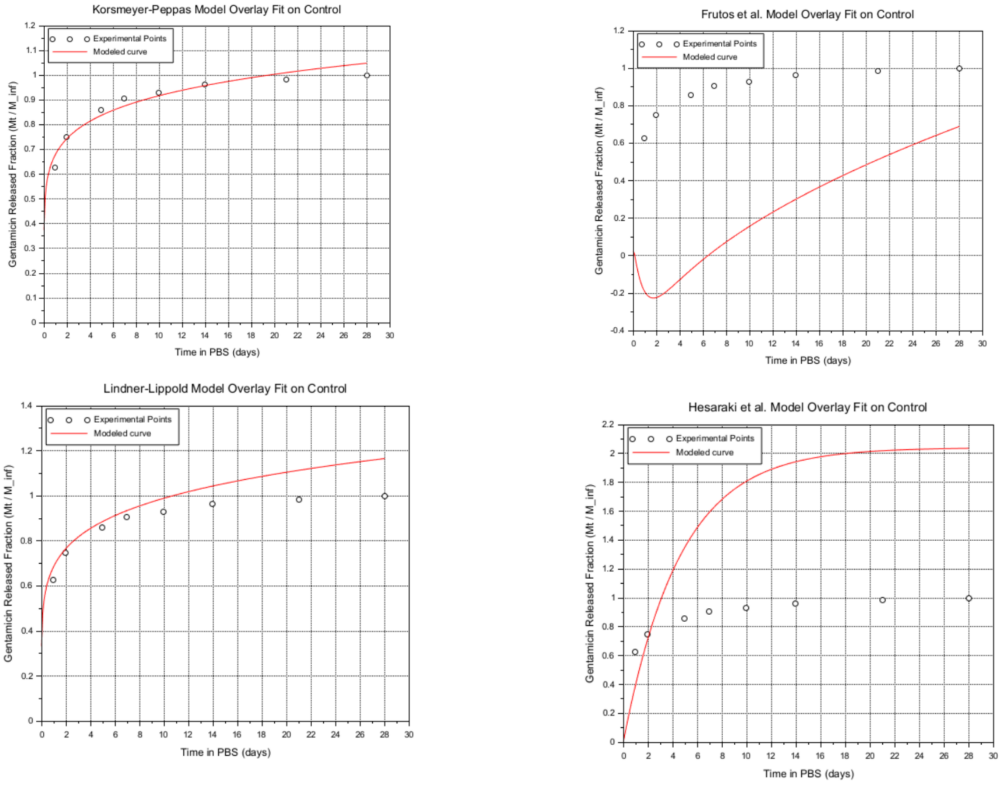

Figure 3.3: Model Overlay Fits for the Control Group

3.4.3 Cross-Group Overlay Plot

The overlay of all seven groups successfully replicates Figure 1 of the reference paper, displaying the raw experimental elution trends across the 28-day period on a single axis.

3.4.4 D_{gent} Bar Chart

The gentamicin diffusion coefficient (D_{gent}) values range from 12.6×10^{-12} m^2/s (15MEPAR) to 28.9×10^{-12} m^2/s (25MEPAR), as visualized in the tool's bar chart.

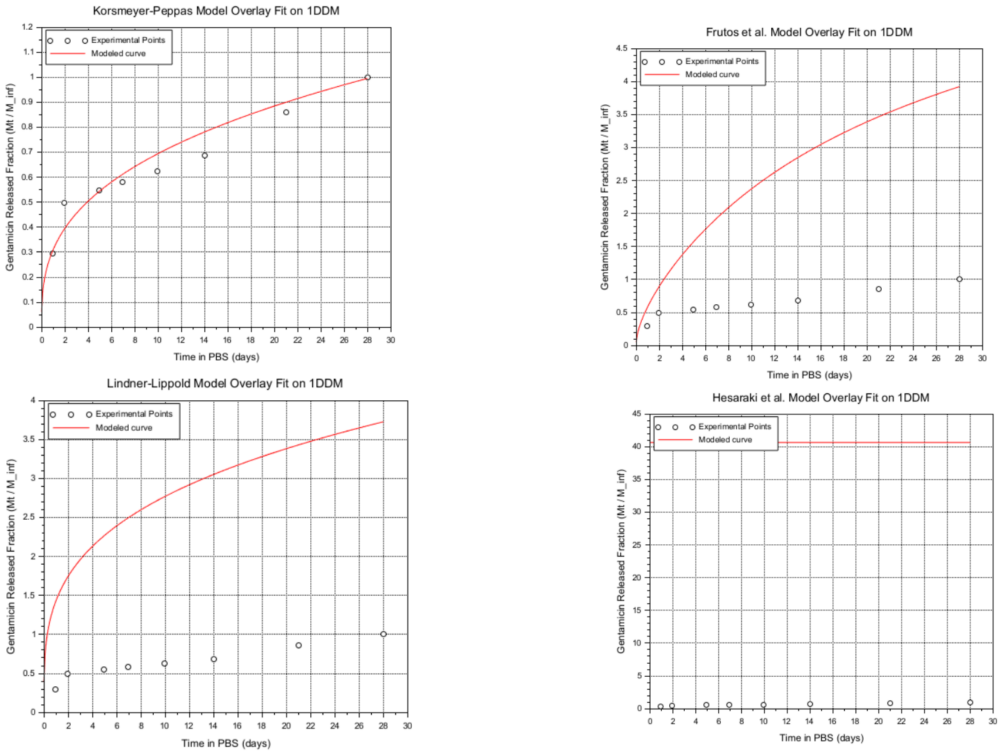

Figure 3.4: Model Overlay Fits for the 1DDM Group

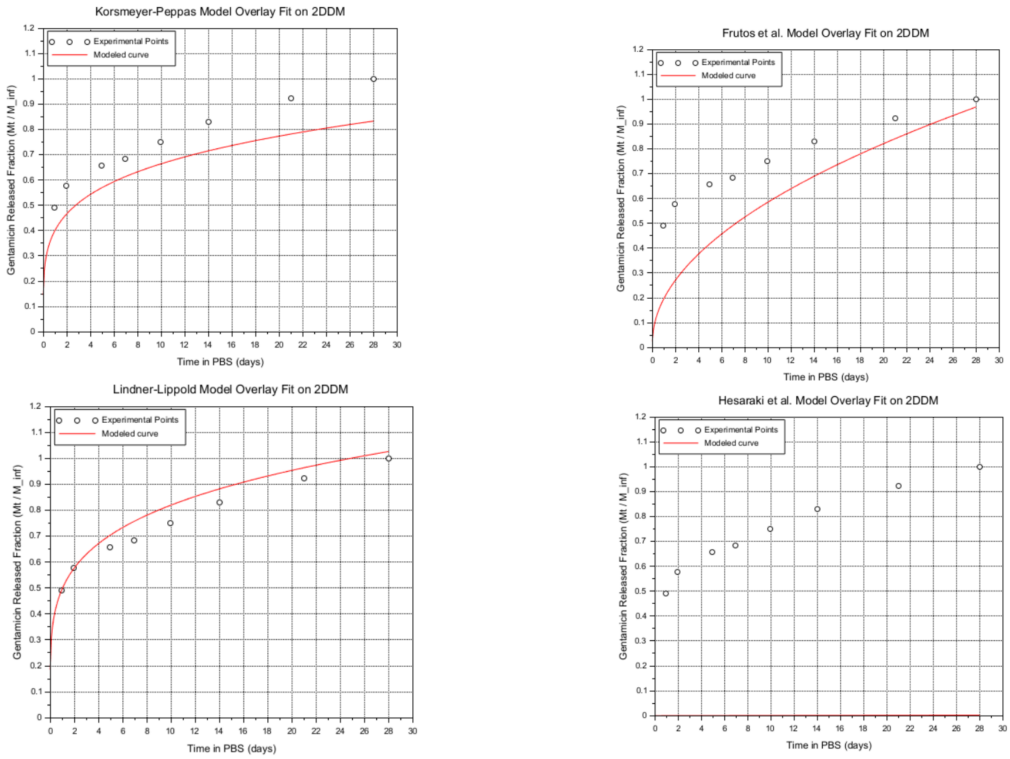

Figure 3.5: Model Overlay Fits for the 2DDM Group

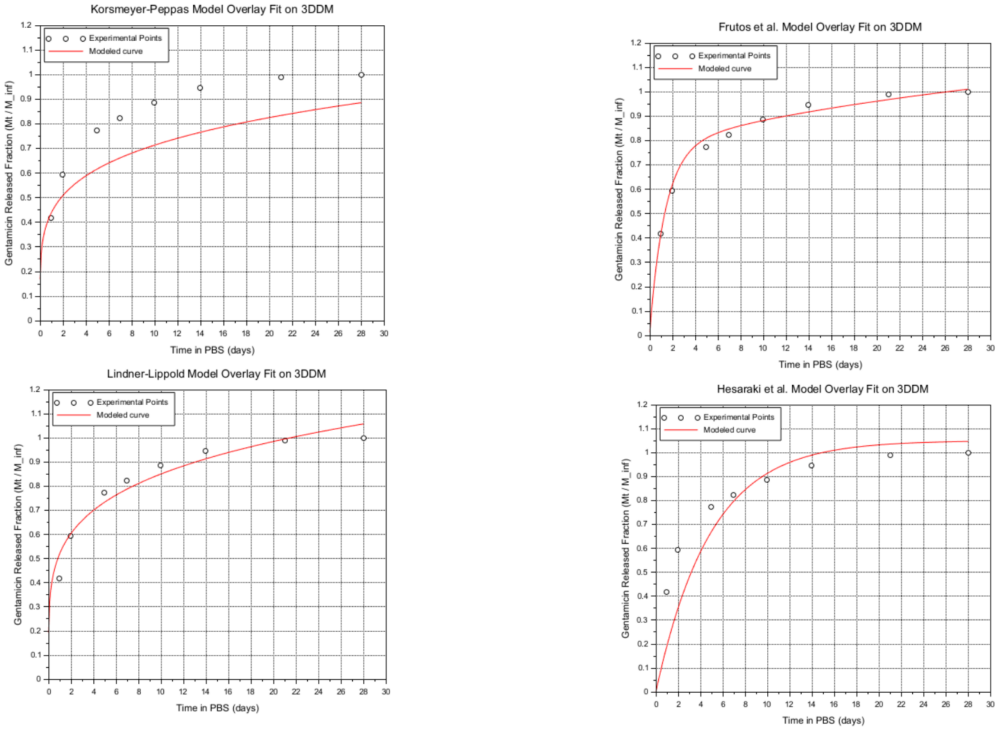

Figure 3.6: Model Overlay Fits for the 3DDM Group

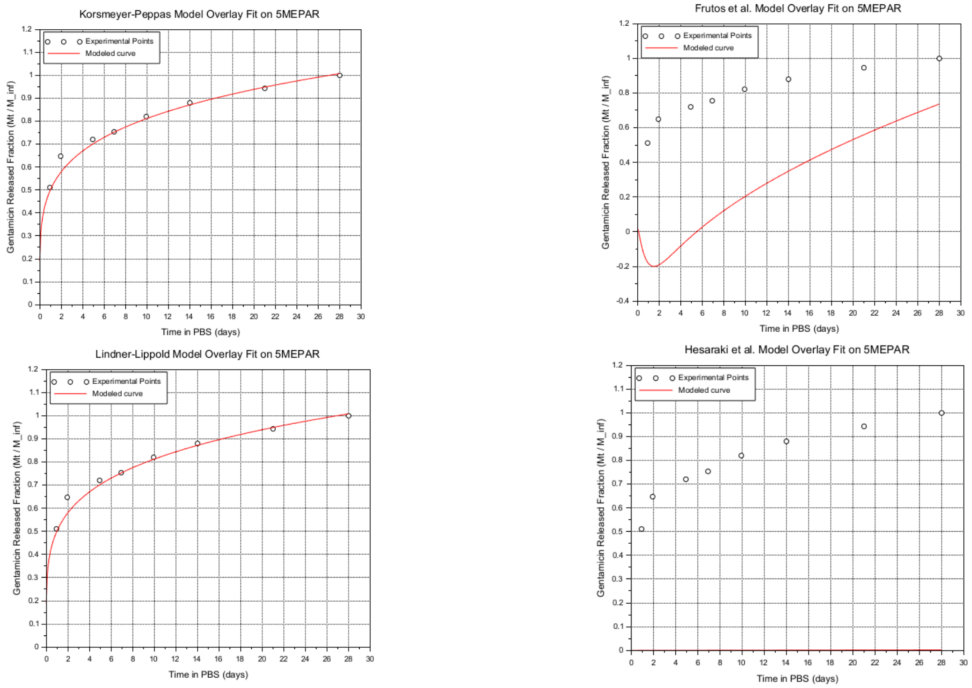

Figure 3.7: Model Overlay Fits for the 5MEPAR Group

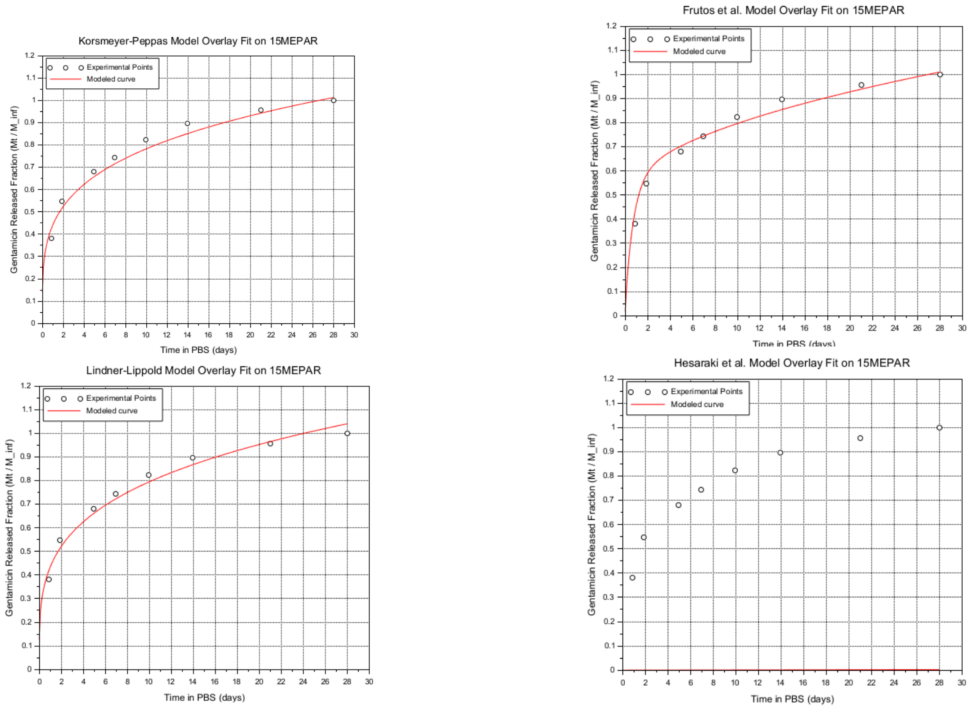

Figure 3.8: Model Overlay Fits for the 15MEPAR Group

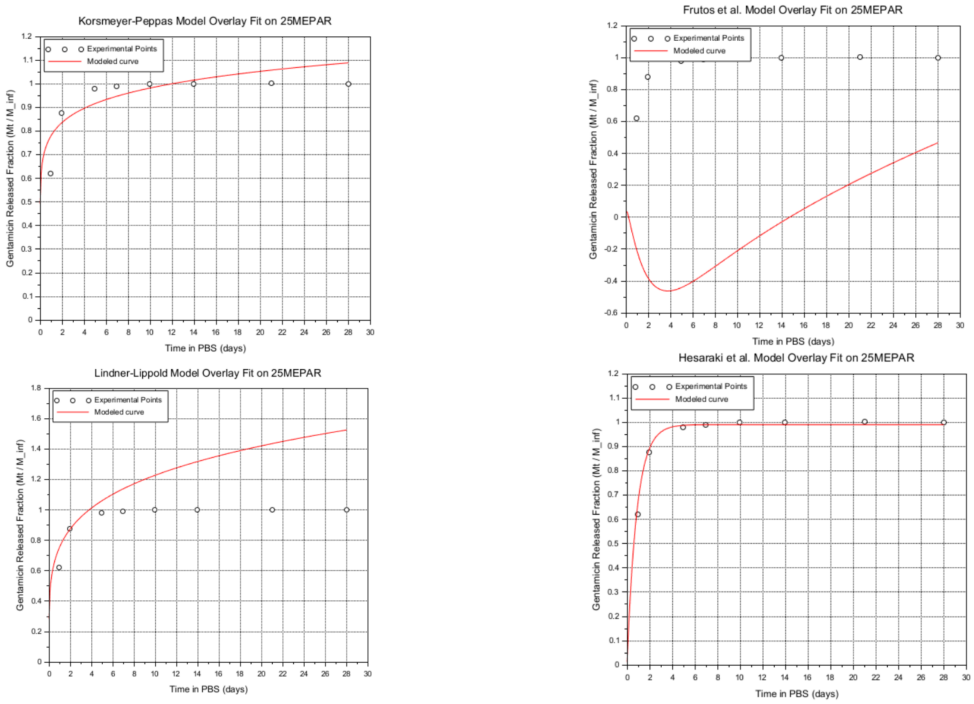

Figure 3.9: Model Overlay Fits for the 25MEPAR Group

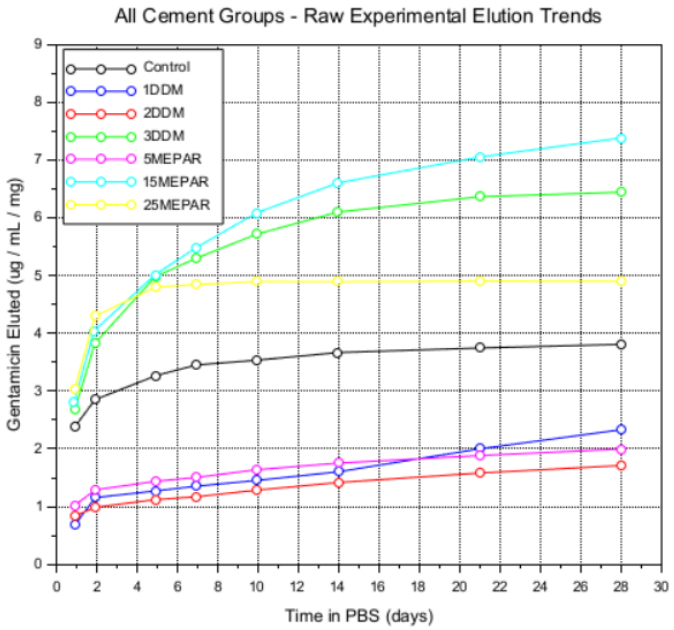

Figure 3.10: All Cement Groups - Raw Experimental Elution Trends

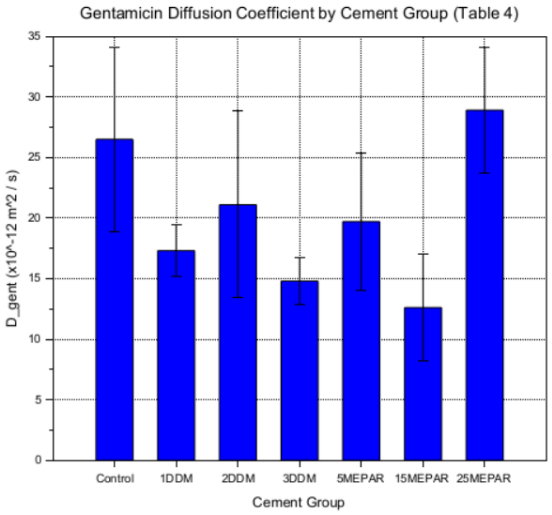

Figure 3.11: Gentamicin Diffusion Coefficient by Cement Group

3.4.5 Adjusted R^2 Values

The table below summarizes the computed adjusted R^2 values across all seven cement groups and the four kinetic equations.

Table 3.1: Adjusted R^2 Values for Kinetic Models Across Cement Groups

Group	**Eq2 AdjR2**	**Eq3 AdjR2**	**Eq4 AdjR2**	**Eq5 AdjR2**
Control	0.9389	0.4945	-38.187	-38.58
1DDM	0.9177	-100.34	-77.74	-38560
2DDM	0.5061	0.9171	-0.6	-20.8
3DDM	0.4613	0.9370	0.9877	0.5388
5MEPAR	0.9677	0.9677	-16.12	-27.27
15MEPAR	0.9716	0.9768	0.9750	-14.38
25MEPAR	0.6488	-4.31	-75.14	0.9833

3.4.6 Conclusions and Project Scope

This case study implemented a Scilab GUI to replicate and visualize the gentamicin elution kinetics results from the reference paper. All four kinetic release models from the paper: Korsmeyer-Peppas (Eq. 2), Lindner-Lippold (Eq. 3), Frutos et al. (Eq. 4), and Hesaraki et al. (Eq. 5) were implemented using the best-fit coefficients from Table 5 across all seven cement formulations. The GUI allows direct visual comparison of how well each model describes the elution behaviour of a given formulation, which is the core purpose of the tool.

As concluded in the paper, D_{gent} values across all seven groups show no significant difference between the experimental formulations and the control, and $n_2 < 0.5$ for Equation 3, which implies that neither MEPAR nor DDM addition meaningfully alters how gentamicin diffuses out of the cement matrix.

Fully implemented from the paper

- All four kinetic model equations (Eq. 2–5) with coefficients exactly as reported in Table 5.
- D_{gent} mean and population SD values from Table 4 for all seven groups were coded.
- Experimental elution data from Figure 1 was digitized via WebPlotDigitizer for all seven groups at all eight time points (1, 2, 5, 7, 10, 14, 21, 28 days).
- Model curve plots (M_t/M_∞ vs time), cross-group overlay of raw elution data replicating Figure 1, and the D_{gent} bar chart with error bars replicating Table 4 were plotted.

Modifications Made

- The paper used actual M_∞ values computed from Equation 1 (cylindrical diffusion governing equation, solved in Wolfram Mathematica) to normalize the experimental data before fitting. Those M_∞ values are not tabulated in the paper. In this implementation, M_∞ is approximated as the day-28 raw eluted value for each group. This introduces a small normalization error for groups still rising at day 28 (Control, 1DDM, 2DDM, 5MEPAR).

- The paper's Figure 2 uses per-specimen M_t/M_∞ experimental data whereas this GUI uses digitized data from Figure 1 since it has not been tabulated in the paper. Since this involves manual identification of data points from a printed graph, the digitized values carry some uncertainty, typically within ± 0.1 to 0.2 units on both axes. As a result, the experimental plot shown in the model fits plots is an approximation of the original data.

Not implemented

- Equation 1 (cylindrical diffusion governing equation) and the associated D_{gent} computation were not implemented. The paper solved this numerically in Mathematica using nonlinear fitting; replicating this would require the raw per-specimen elution data in absolute μg, which is not available.

- The nonlinear least-squares fitting routine used to obtain the Table 5 coefficients (OriginPro 8.6) was not reimplemented, and coefficients are hardcoded directly from the paper.

- Statistical analysis (Kruskal-Wallis test with Bonferroni correction, SAS Version 11.5) comparing D_{gent} and n_2 across groups was not reimplemented.

Chapter 4

Case Study 3: Comparative Study of Linear and Nonlinear Swelling Kinetics in Substrate Constrained Hydrogels

4.1 Abstract

This case study implements the constrained swelling problem from Bouklas and Huang's comparison of nonlinear and linear poroelasticity theories. A hydrogel layer bonded to a rigid substrate swells only through the thickness while solvent diffuses in from one exposed face. The nonlinear stretch field is found by solving a nonlinear diffusion equation in Scilab using an explicit finite difference scheme, with the surface boundary value fixed by solving a nonlinear algebraic equation using fsolve and a no-flux condition at the substrate.

The resulting thickness swelling curves are compared against the linear poroelasticity solution, computed as a truncated infinite series, using the same initial swelling ratio and material parameters as the paper. The case study reproduces the thickness-versus-time curves and equilibrium swelling ratio comparison shown in Fig. 2a, 3a, 6 and 7 of the paper, showing where the linear theory's prediction departs from the nonlinear one as the swelling ratio grows.

4.2 Problem Statement

Hydrogel swelling is a transient process coupling solvent diffusion and mechanical deformation. Traditionally, this is modeled using linear poroelasticity, which assumes infinitesimal deformations and constant material properties. However, real hydrogels undergo massive volumetric changes that dynamically alter their internal solvent mobility. The core problem is that linear theory fails to accurately predict swelling behavior during large deformations, particularly when the gel is laterally constrained and swells in only one dimension.

To address this limitation, the project applies a nonlinear continuum theory based on Flory-Rehner thermodynamics that correctly accounts for stretch dependent material properties. To demonstrate exactly where and how the two frameworks diverge, we developed a numerical simulation in Scilab. The classical linear theory was evaluated using its exact analytical Fourier series solution, while the complex nonlinear theory was solved using an explicit one-dimensional Finite Difference Method (FDM). By generating graphs of the spatial stretch profiles, thickness swelling kinetics, and equilibrium limits across various initial swelling states and chemical interaction parameters, this project maps the exact physical thresholds where the linear poroelasticity assumption breaks down.

4.3 Flowchart

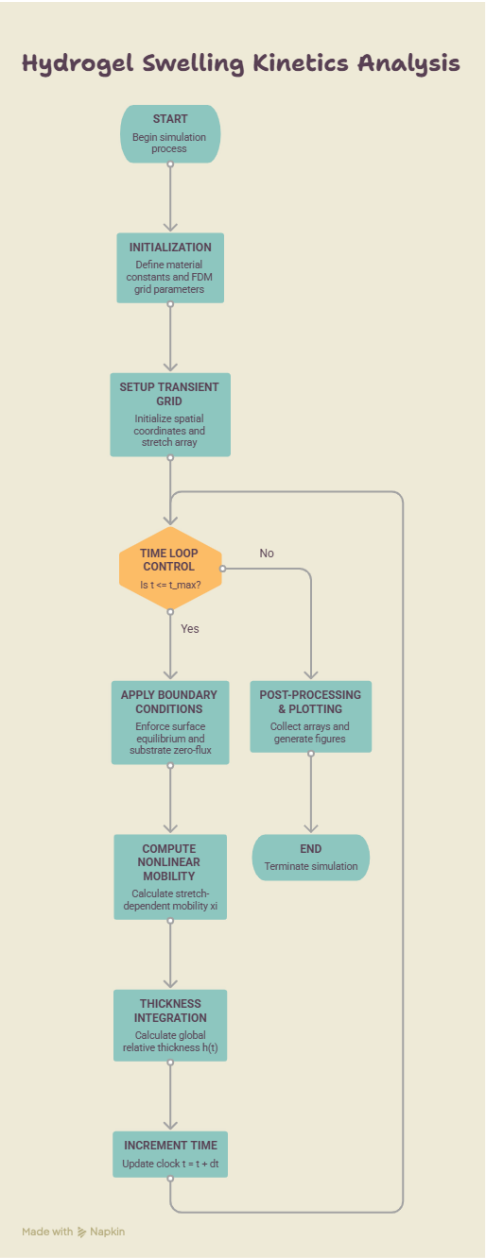

Figure 4.1: Hydrogel Swelling Kinetics Analysis Flowchart

4.4 Results and Discussion

The data collected from the Scilab simulation provides a comprehensive view of the transient and equilibrium swelling behaviors of the substrate-constrained hydrogel layer. The results are categorized into spatial profiles, kinetic swelling rates, and direct comparisons between the linear and nonlinear theories.

4.4.1 Spatial Distribution of Stretch (Figure 2a)

The first simulation tracks how the local stretch ratio (λ_2) distributes itself across the normalized thickness coordinates of the hydrogel (X_2/H) at various stages of time (t/τ_1). The bottom surface at $X_2/H = 0$ is fixed to the rigid substrate, and the top surface at $X_2/H = 1$ is exposed to the solvent.

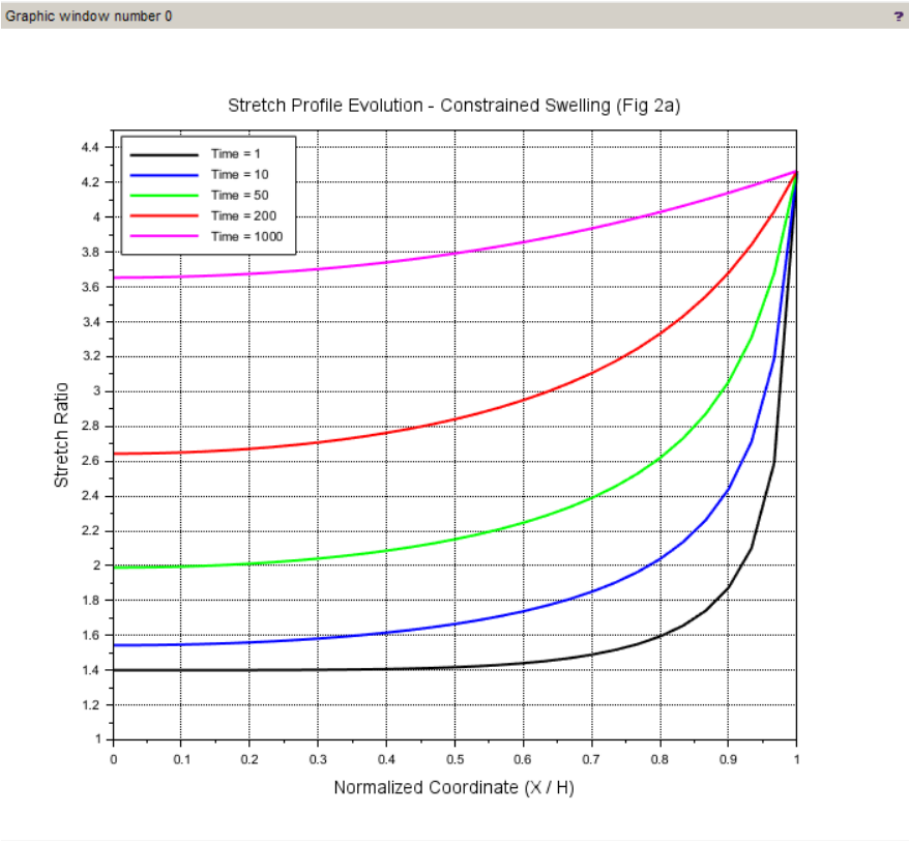

Figure 4.2: Evolution of local stretch profiles across the normalized hydrogel thickness at increasing time intervals

At the early stages of swelling ($t/\tau_1 \to 0$), a highly localized, steep gradient develops near the exposed upper surface ($X_2/H = 1$). This occurs because the top surface reaches instantaneous chemical equilibrium with the solvent reservoir immediately, while the deeper layers of the gel remain completely unswollen at their initial stretch ($\lambda_0 = 1.4$). As time progresses, the solvent penetrates deeper into the network via diffusion. The steep gradient gradually smooths out until the stretch profile becomes completely uniform throughout the entire thickness of the layer, approaching the final equilibrium stretch (λ_∞).

4.4.2 Thickness Swelling Kinetics for Varying Interaction Parameters (Figure 3a)

The second simulation evaluates the macroscopic thickness swelling ratio $(h(t)/h_0)$ over a normalized time window for three distinct Flory-Huggins interaction parameters ($\chi = 0.2$, 0.4, and 0.6).

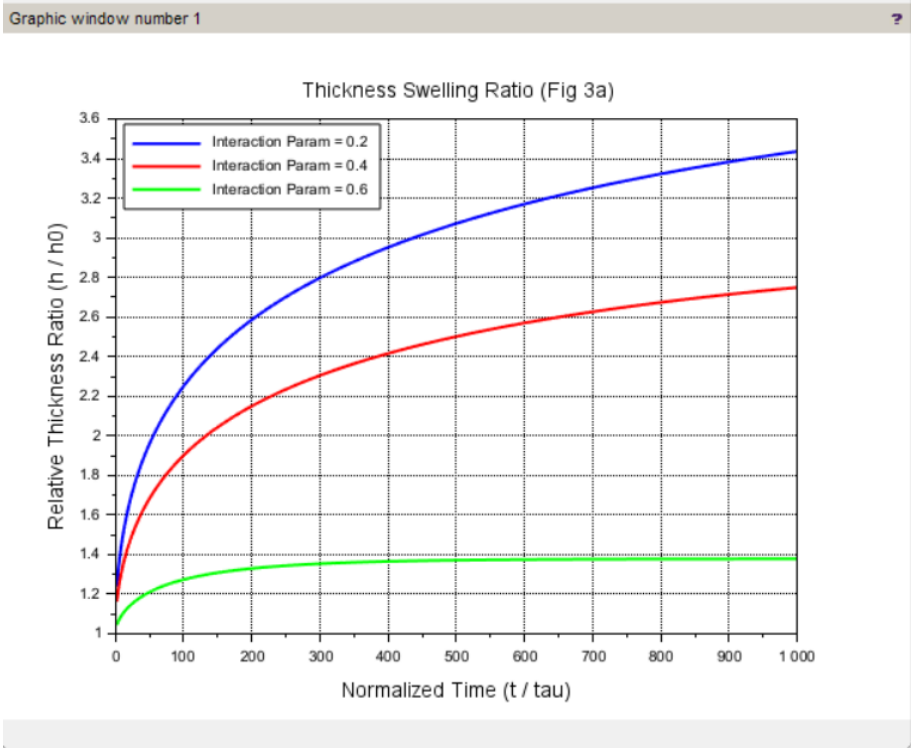

Figure 4.3: Relative thickness swelling ratio as a function of time for different values of the interaction parameter chi, including horizontal dashed equilibrium lines

The interaction parameter χ represents the chemical affinity between the polymer network and the solvent molecules. When $\chi = 0.2$, the polymer has a very high affinity for the solvent, absorbing a massive amount of fluid and causing the thickness curve to plateau at a high relative value of 4.0. When χ is increased to 0.4 and 0.6, the chemical affinity decreases, causing the relative thickness expansion to saturate at lower values of 3.05 and 1.38, respectively. Additionally, the time required to reach a stable plateau increases significantly as χ decreases. This happens because a larger volume of incoming solvent requires a longer total diffusion time to distribute uniformly throughout the network.

4.4.3 Transient Divergence Between Linear and Nonlinear Theories (Figure 6)

This plot directly compares the transient expansion curves generated by the linear poroelasticity theory (solved via an analytical Fourier series) against the nonlinear continuum theory (solved via the FDM algorithm) across different initial swelling conditions.

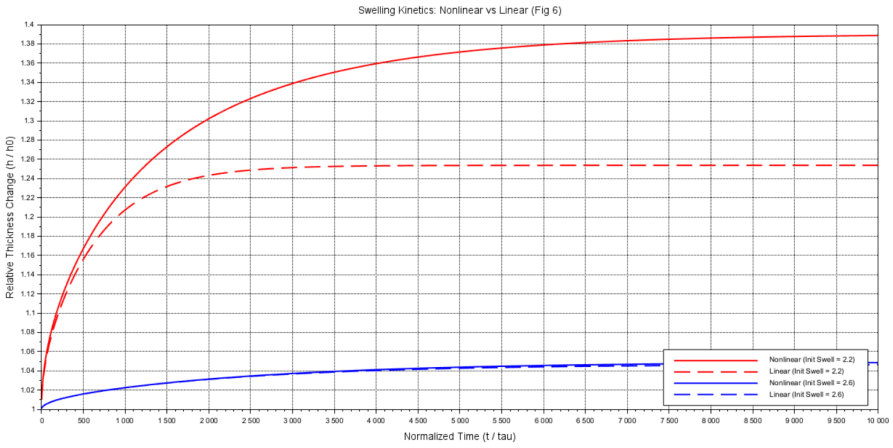

Figure 4.4: Comparison of transient thickness changes over time between the linear analytical solution and the nonlinear numerical solution for different initial swelling states.

When the system undergoes small deformations from its initial state, the linear and nonlinear curves track tightly together, demonstrating that the two mathematical frameworks are consistent under small perturbations. However, during large deformations, the two curves diverge significantly. The linear theory assumes that the diffusion coefficient and elastic constants remain rigidly fixed, leading to a constant, predictable swelling rate. In contrast, the nonlinear theory captures the physical reality that as the gel expands, the polymer network dilates, which dynamically increases the local solvent mobility. Consequently, the nonlinear model shows a faster rate of expansion and a different final saturation point than the linear model.

4.4.4 Global Equilibrium Convergence and Divergence Map (Figure 7)

The final result maps out the final steady-state thickness ratios predicted by both theories across a broad spectrum of initial swelling states (λ_0).

This global map illustrates the physical boundary conditions where linear poroelasticity becomes completely invalid. At initial stretch states close to equilibrium where the net deformation is minimal, the percentage error between the two models is negligible. However, as the gap between the initial state and the final equilibrium expands, the linear theory completely breaks down. Because it fails to account for large-strain geometric constraints and non-constant chemical potentials, the linear model introduces unacceptable errors in predicting final volumes. This confirms that for real-world hydrogel applications experiencing large volumetric changes, the nonlinear framework is strictly necessary.

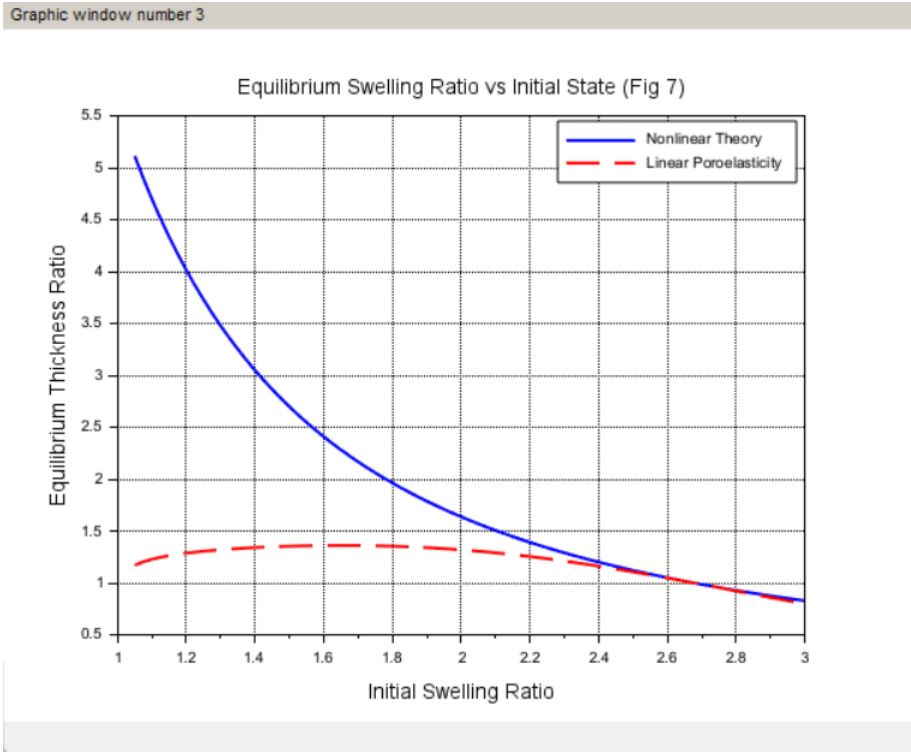

Figure 4.5: Global divergence map showing the final equilibrium thickness values predicted by the linear and nonlinear theories across a wide range of initial stretch states

4.4.5 Implementation Scope and Model Limitations

This case study performs a partial replication of Bouklas and Huang (2012), focusing only on the substrate-constrained one-dimensional swelling problem and reproducing Figures 2a, 3a, 6 and 7 using Scilab. Several aspects of the original paper were intentionally left out of this project. The simulation does not model the freestanding hydrogel layer described in Section 4.2, which lacks constraints and expands in all three dimensions. The Scilab script also ignores mechanical surface wrinkling, buckling, or creasing instabilities caused by high transient stresses near the surface. Instead, it assumes the gel layer remains perfectly flat throughout the swelling process.

The implemented model operates under specific physical and numerical limitations. Physically, it assumes a strictly 1D geometry. This assumption is only valid if the lateral width and length of the gel are much larger than its thickness ($L, W \gg H$), allowing us to ignore edge effects and shear stresses at the boundaries. Thermodynamically, the model assumes ideal Flory-Huggins mixing and a constant crosslink density. Numerically, the explicit Finite Difference Method (FDM) is tightly bound by the Courant-Friedrichs-Lewy (CFL) stability condition. If the time step (dt) is increased too much relative to the spatial step (dX), the explicit integration scheme becomes unstable and the numbers rapidly go upto infinity.

4.4.6 Numerical Analysis and Deviations

The curves generated by the Scilab simulation track the exact same physical trends and reach identical steady-state plateaus as those published by Bouklas and Huang (2012), but they do not overlap with absolute mathematical perfection. These small discrepancies are normal results of spatial and temporal discretization. While the original paper likely used an advanced or adaptive numerical solver, this Scilab implementation relies on a fixed spatial grid of 50 nodes ($NX = 50$).

The most noticeable differences happen at the very beginning of the swelling process (t tending to zero). The sudden step-change in solvent concentration at the exposed boundary creates an incredibly sharp spatial gradient. Because a uniform 1D FDM grid uses a fixed spatial step size, It experiences localized mathematical truncation errors when trying to resolve this steep jump. This causes the minor visual deviations in the early-time curve paths seen in Figures 2a and 6.

Minor deviations also come from the numerical root-finding process. The fsolve function calculates the boundary condition within a set convergence tolerance of 10^{-10}. Any tiny rounding error in this root slightly alters the fixed value at the top node of the mesh. Over millions of iterations inside the time loop, these minute differences accumulate, causing very small variations in the transient swelling speed before the system successfully levels out at the correct final equilibrium.

Chapter 5

Conclusion

The **FOSSEE Summer Fellowship** has been an immensely rewarding experience, marked by a range of learning opportunities and notable accomplishments. Across the three case studies I explored numerous topics ranging from antibiotic kinetics release kinetics to geostationary satellite trajectory simulation.

In **Case Study 1**, the modeling and simulation of satellite orbit dynamics and orbit controllers using Scilab and Xcos provided a practical validation of orbital station-keeping strategies. By evaluating both a fully controllable two-thrust system and a single-input tangential fallback strategy, the study successfully demonstrated the physical trade-offs between full state correction and permanent radial drift, confirming the robustness of feedback control in counteracting orbital perturbations.

Case Study 2 investigated the drug release kinetics of antibiotic-loaded PMMA bone cements through an interactive Scilab GUI. The comparative analysis of four mathematical release models across seven different formulations clearly visualized the underlying physical diffusion mechanisms. The results highlighted the limitations of standard kinetic equations in perfectly predicting real-world elution behavior.

In **Case Study 3**, the comparative numerical study of linear and nonlinear swelling kinetics in substrate-constrained hydrogels provided a rigorous evaluation of polymer deformation theories. By mapping the transient spatial stretch profiles and equilibrium limits, the analysis revealed exactly where classical linear poroelasticity breaks down under large volumetric changes, underscoring the necessity of nonlinear continuum models for accurately predicting high-swelling hydrogel behavior in practical applications.

To conclude, not only my knowledge of computational tools has enhanced, but has also equipped me for future pursuits in research and academia. I am grateful for the opportunities, mentorship, and insights gained, all of which have significantly advanced my professional development. I am excited to apply these skills and insights.

Chapter 6

Key Learnings and Technical insights

This fellowship provided hands-on experience in translating mathematical models and engineering concepts into working software. The major technical and practical skills gained during the project are summarized below.

6.1 Scilab and Xcos Programming

- **Coding and Solvers:** Developed a strong foundation in Scilab syntax, utilizing numerical tools like `ode()` for differential equations and `fsolve` for solving implicit, nonlinear algebraic equations.
- **Xcos Simulations:** Learned to build block-based dynamic simulations, implement custom physics equations through expression blocks, and integrate random noise generators to model real-world perturbations.
- **GUI Development:** Gained practical experience designing interactive user interfaces. Learned how to link dashboard controls to real-time plotting routines and performance metrics (RMSE and R^2) without breaking application stability.

6.2 Replicating Academic Research

- **Data Extraction:** Learned to use WebPlotDigitizer to digitize and extract raw data coordinates from printed research graphs, while accounting for the natural margins of error in manual extraction.
- **Problem-Solving with Incomplete Data:** Realized that papers often omit intermediate variables. Learned to make logical engineering approximations, such as using day-28 elution values to substitute for missing equilibrium constants (M_∞).

6.3 Case Study Engineering Insights

- **Orbital Dynamics:** Visualized how space forces cause satellite drift and analyzed how single-thrust versus two-thrust feedback setups affect positioning errors and recovery times.
- **Elution Kinetics:** Studied how mass transfer occurs in bone cement, observing how chemical additives lower setting heat without altering the core diffusion mechanism of the antibiotic.
- **Hydrogel Mechanics:** Explored the physics of large polymer deformations, using Flory-Rehner thermodynamics to map exactly where traditional linear poroelasticity theory fails during massive volumetric swelling.

Chapter 7

References

- M. A. Malik, G. A. Zaidi, I. Aziz and S. Khushnood, "Modeling and simulation of an orbit controller for a communication satellite," Proceedings. IEEE International Multi Topic Conference, 2001. IEEE INMIC 2001. Technology for the 21st Century., Lahore, Pakistan, 2001, pp. 246-251, doi: 10.1109/INMIC.2001.995345.

- Lewis, G. and Li, L. (2019) Kinetics of Elution of Gentamicin from a GentamicinLoaded PMMA Bone Cement. World Journal of Engineering and Technology, 7, 418428

- Bouklas, N., & Huang, R. (2012). Swelling kinetics of polymer gels: comparison of linear and nonlinear theories. Soft Matter, 8(31), 8194–8203.

- Scilab Enterprises. "Scilab: Free and Open Source software for numerical computation." Available at: https://www.scilab.in/.

- FOSSEE Project, IIT Bombay. "Free/Libre and Open Source Software for Education (FOSSEE)." Available at: https://fossee.in/.

- Scilab case studies. Available at: https://scilab.in/case-study-portal/casestudy-project.